# Dip moveout for converted-wave (P-SV) data

**Mark P. Harrison**

## ABSTRACT

The problems of reflection-point smearing, or dispersal, and changes in apparent stacking velocity introduced by reflector dip are well known for conventional (P-P) data. An expression for the converted-wave (P-SV) dispersal within a common-conversion-point (CCP) gather is derived here. It is found that the P-SV dispersal is asymmetric about zero dip, with greater dispersal for data acquired in the down-dip direction than in the up-dip direction. Calculations of P-SV apparent velocity vs. dip angle also show an asymmetry about zero-dip. Because of this, conventional P-P dip moveout (DMO) is not appropriate for converted-wave data.

The DMO concept is here extended to P-SV data by using geometrical optics to construct the P-SV zero-offset mapping function for the constant-velocity case. It is shown that, as in the P-P case, an exact solution to the time response curves for a P-SV DMO operator can be obtained. This solution contains within it the equation of the P-P DMO traveltime curves as a special case. The time-response curves for P-SV DMO operators generated using this equation show the operators to be asymmetric, with the location of maximum time on the curves corresponding to the position of the zero-dip conversion point. Application of P-SV DMO moves the data samples horizontally to the proper conversion points, performing a conversion-point rebinning of the data. This leads to a new method for computing the location of the zero-dip conversion point. Application of P-SV DMO to synthetic data using an integral-summation algorithm is found to greatly reduce the dispersal within CCP gathers. This gives a visible improvement in the amplitude and continuity of dipping horizons.

## INTRODUCTION

The difficulties introduced by recording data over dipping reflectors have been known for some time for the conventional (P-P) case. Levin (1971) showed that, at non-zero offset, the reflection point for data from a dipping interface is displaced away from the midpoint. This gives rise to a smearing, or dispersal, of the data within a common-midpoint gather, which increases with both offset and reflector dip. This dispersal, in turn, gives rise to an increase in the apparent NMO velocity necessary to properly flatten the dipping event. This apparent velocity is given by Levin (1971) as

$$V_{app} = \frac{V}{\cos\theta}, \qquad (1)$$

where $V_{app}$ is the apparent velocity, V is the true medium velocity and $\theta$ is the reflector dip. If data with more than one dip is present at any two-way time and common-midpoint location, then only one dip can be optimally stacked. The movement of the reflection point away from the midpoint with increasing dip and offset causes the dipping data to be attenuated by the stacking process (Judson et al., 1978). Post-stack migration, which

assumes zero-offset data, will be unable to properly image any dipping, non-zero-offset data which survives the stacking process, as the data are displaced away from the true zero-offset position by an amount depending on both the dip and offset. Dip moveout, or DMO, attempts to overcome these problems.

The geometric optics approach to DMO attempts to generate the locus of points for every datum sample such that, when zero-offset migration is applied, the resulting migrated locus of points will be the same as that obtained by performing prestack migration. It therefore attempts to create for any offset the equivalent zero-offset data, so that post-stack migration will be appropriate (Deregowski and Rocca, 1981). The idea of applying DMO to P-P data was first introduced by Judson et al. in 1978, and initially met with limited technical success. The idea was extended by Yilmaz and Claerbout (1980) in the form of partial prestack migration. Deregowski and Rocca (1981) derived the zero-offset mapping equation for the P-P case, and used it to generate time-domain "smear stack" impulse responses for the P-P DMO operator. Hale (1984) devised a Fourier-transform algorithm that was numerically accurate for all dip angles in a single layer medium. Because Hale's method requires a transform that cannot be implemented using the FFT, it is very expensive to perform. Other methods using integral-summation algorithms, in which impulse response functions are generated and summed (Deregowski, 1985), or log-stretch algorithms (Notfors and Godfrey, 1987) have been more computationally effective.

The first part of this paper is concerned with the behavior of P-SV converted data in areas of dip. If the apparent velocity and common-conversion-point (CCP) dispersal for P-SV data are similar to that of P-P data, then a modified P-P DMO could perhaps be applied to P-SV data. It is found, however, that this is not the case. In the second part of the paper, a zero-offset mapping (DMO) equation is derived using geometric optics. This equation is used to implement an integral-summation algorithm (Deregowski, 1985) to apply DMO to some synthetic converted-wave data.

## P-SV DISPERSAL

Dispersal within a CMP gather for P-P data is defined (Levin, 1971) as the distance $\Delta$ that the actual reflection point will move away from the zero-offset reflection point as the reflector dip and source-to-receiver offset are changed. For the P-P case, it can be shown (Levin, 1971) that this dispersal is given by

$$\Delta = \frac{h^2}{d} \cos\theta \sin\theta \tag{2}$$

where

$2h$ = total source-to receiver offset.

$\theta$ = dip angle of the reflector.

$d$ = distance from the surface CMP location to the zero-offset reflection point on the dipping interface.

From equation 2, it is seen that the magnitude of the dispersal within a CMP gather is symmetric about zero-dip; there is no difference between positive and negative dip angles.

Using similar definitions, it is possible to set up the problem for the P-SV case. The dispersal will now be the movement within a CCP away from the zero-offset conversion point. From Figure 1, it can be seen that the dispersal is given by

$$\Delta = -\delta \cos\theta \tag{3}$$

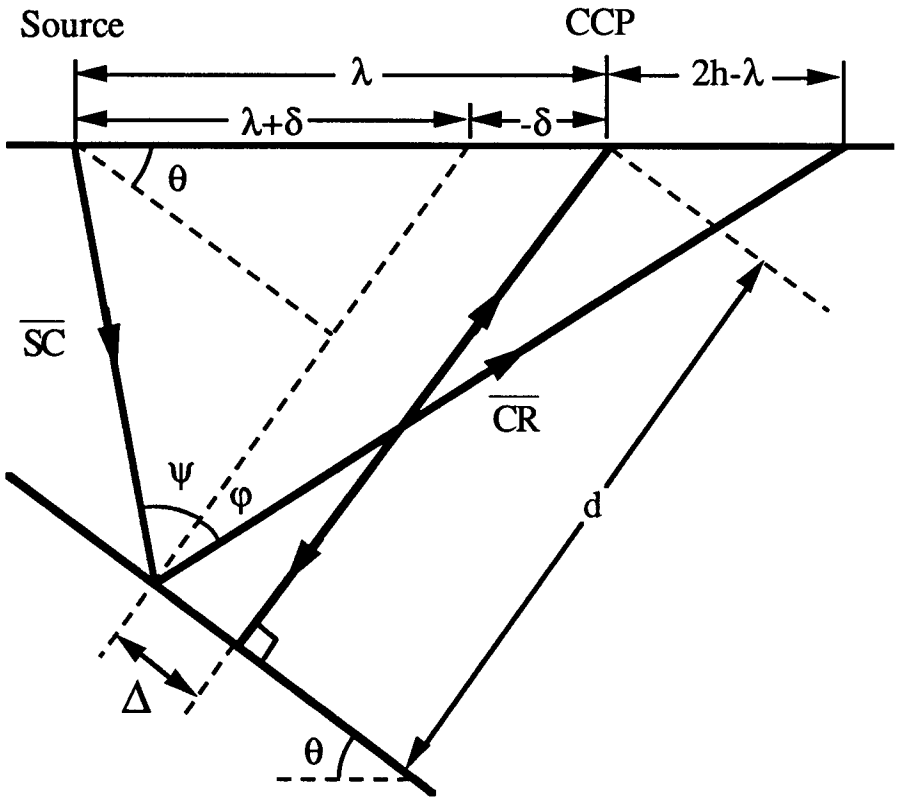


Fig. 1. Raypath geometry for conversion from a dipping layer.

where δ is the horizontal surface displacement away from the CCP position. It can be shown using simple geometry that

$$\overline{SC} = \sqrt{(d - \lambda \sin\theta)^2 + (\lambda+\delta)^2\cos^2\theta}\ , \tag{4}$$

$$\overline{CR} = \sqrt{[d + (2h-\lambda)\sin\theta]^2 + [2h-(\lambda+\delta)]^2\cos^2\theta}\ , \tag{5}$$

and

$$\tan\varphi = \frac{[2h-(\lambda+\delta)]\cos\theta}{d + (2h-\lambda)\sin\theta}\ ,$$

which can be rearranged to give

$$(\lambda+\delta) = 2h - \frac{d + (2h-\lambda)\sin\theta}{\cos\theta}\tan\varphi\ . \tag{6}$$

From Snell's Law, the ray parameter must be constant for both the incident and reflected rays, giving

$$\frac{\sin\psi}{\alpha} = \frac{\sin\varphi}{\beta}$$

or

$$\tan\varphi = \frac{\sin\psi}{\sqrt{\gamma^2 - \sin^2\psi}}, \quad \gamma = \frac{\alpha}{\beta}. \tag{7}$$

From Figure 1, it can be seen that

$$\sin\psi = \frac{(\lambda+\delta)\cos\theta}{\overline{SC}}$$

$$= \frac{(\lambda+\delta)\cos\theta}{\sqrt{(d - \lambda\sin\theta)^2 + (\lambda+\delta)^2\cos^2\theta}}.$$

Substituting this result into equation 7 gives

$$\tan\varphi = \frac{(\lambda+\delta)\cos\theta}{\sqrt{\gamma^2(d - \lambda\sin\theta)^2 + (\gamma^2-1)(\lambda+\delta)^2\cos^2\theta}},$$

and equation 6 becomes

$$(\lambda+\delta) = 2h - \frac{(\lambda+\delta)[d + (2h-\lambda)\sin\theta]}{\sqrt{\gamma^2(d - \lambda\sin\theta)^2 + (\gamma^2-1)(\lambda+\delta)^2\cos^2\theta}}.$$

Rationalizing this result and collecting terms gives the following quartic equation for $(\lambda+\delta)$;

$$\begin{aligned}&(\gamma^2-1)(\lambda+\delta)^3[(\lambda+\delta)-4h]\cos^2\theta \\ &+ \{\gamma^2(d - \lambda\sin\theta)^2 + (\gamma^2-1)4h^2\cos^2\theta - [d + (2h-\lambda)\sin\theta]^2\}(\lambda+\delta)^2 \\ &- 4h\gamma^2(d - \lambda\sin\theta)^2(\lambda+\delta) + 4h^2\gamma^2(d - \lambda\sin\theta)^2 = 0.\end{aligned} \tag{8}$$

For a given source-to-receiver offset **2h** and zero-offset reflector distance **d**, the location of the zero-dip conversion point, $\lambda$, can be computed using, for example, the result given in Tessmer and Behle (1988). For any reflector dip angle, equation 8 can then be solved to give $\delta$, from which the dispersal can be computed using equation 3. The results of doing this for two different offset-to-depth ratios, with dip angles ranging between ±90°, are shown in Figure 2. For comparison, the P-P dispersal values computed using equation 2 are also plotted in the figure. A compressional velocity of 3000 m/s and a shear velocity of 1500 m/s were used in all the computations.

From Figure 2, it is seen that for data acquired by shooting in the positive-dip (down-dip) direction, the CCP dispersal is larger than the CMP dispersal, whereas for data acquired in the negative-dip (up-dip) direction, the opposite is true. Because any DMO operation that is applied to the converted data must correct for CCP dispersal, the DMO operator must itself be asymmetric. This indicates that conventional P-P DMO cannot be expected to work correctly on P-SV data.

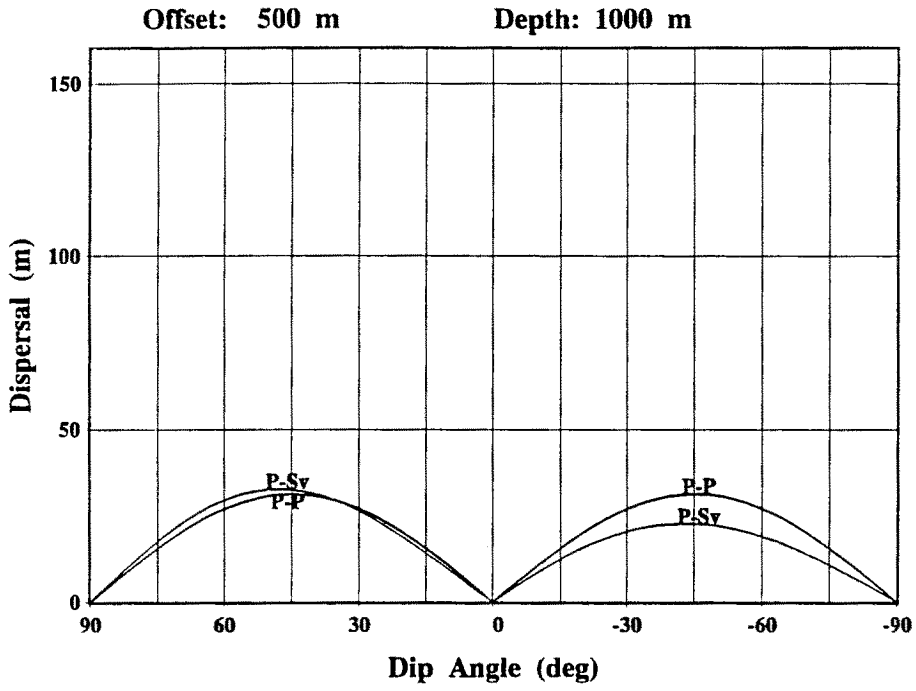


(a)

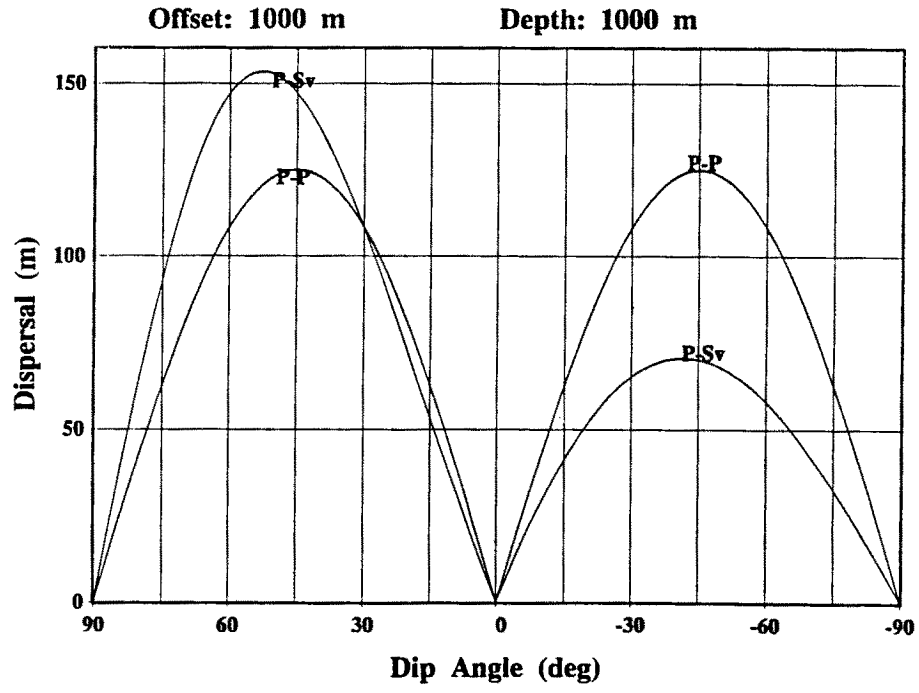


(b)

Fig. 2. P-P and P-SV dispersal curves for a reflector depth of 1 km and source-to-receiver offsets of a) 0.5 km and b) 1.0 km.

## P-SV APPARENT SLOWNESS

From Figure 1, it can be seen that the total source-to-receiver traveltime will be the sum of the time to travel from the source to the conversion point along the path $\overline{SC}$ at velocity $\alpha$, and the time to travel from the conversion point back to the receiver along the path $\overline{CR}$ at velocity $\beta$, or

$$t = \frac{\overline{SC}}{\alpha} + \frac{\overline{CR}}{\beta} .$$

Using equations 4 and 5, this becomes

$$t = \frac{\sqrt{(d - \lambda \sin\theta)^2 + (\lambda+\delta)^2\cos^2\theta}}{\alpha} + \frac{\sqrt{[d + (2h-\lambda)\sin\theta]^2 + [2h-(\lambda+\delta)]^2\cos^2\theta}}{\beta} . \qquad (9)$$

It is known (Tessmer and Behle, 1988) that even for zero-dip, equation 9 cannot be rearranged to give an exact expression in the form of the conventional NMO equation, as can be done in the P-P case. In order to assess the effect of reflector dip on stacking velocity, it is possible to obtain an expression for the apparent slowness by simply rearranging the conventional NMO equation. In terms of slowness s, the NMO equation becomes

$$t^2 = t_0^2 + 4h^2s^2,$$

where $t_0$ is the zero-offset traveltime, t is the total traveltime given by equation 9, and 2h is again the total source-to-receiver offset. This can be rearranged to give the following expression for the apparent slowness;

$$s = \frac{\sqrt{t^2 - t_0^2}}{2h} . \qquad (10)$$

Using equation 8 to compute $\delta$ and equation 9 to compute t, the apparent slowness can be calculated for any dip angle from equation 10. The result indicates how the stacking velocity, which will be the reciprocal of slowness, changes with reflector dip angle. Apparent slowness calculations for the same offset-to-depth ratios used in Figure 2 are shown in Figure 3. From this figure, it is seen that the apparent slowness (velocity) curves for P-SV data are asymmetric about zero-dip. This is in contrast to the P-P case, where the apparent slowness is seen from equation 1 to be a cosine curve, symmetric about zero dip. Also, for part of the slowness curve in the range of about 65 to 90 degrees, the slowness becomes imaginary. This means that the total traveltime is actually less than the zero-offset traveltime; something that does not happen for P-P data. Events within a gather converted by a reflector with dip in this range will appear to be over-corrected even before any NMO has been applied.

Data acquired using split spreads would see a dipping interface as having positive dip on one side of the spread, and negative dip on the other. A CCP gather containing both sides of the spread would therefore have two different apparent NMO velocities for the event, because of the asymmetry seen in Figure 3. Even for a single event, this suggests that it may not be possible to properly NMO-correct the gather with a single apparent stacking velocity.

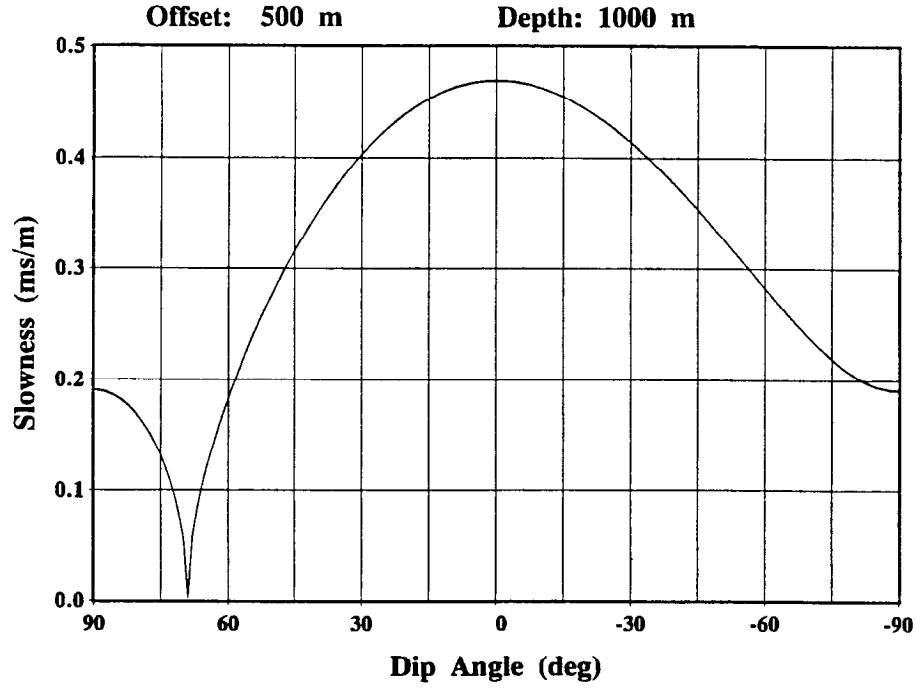


(a)

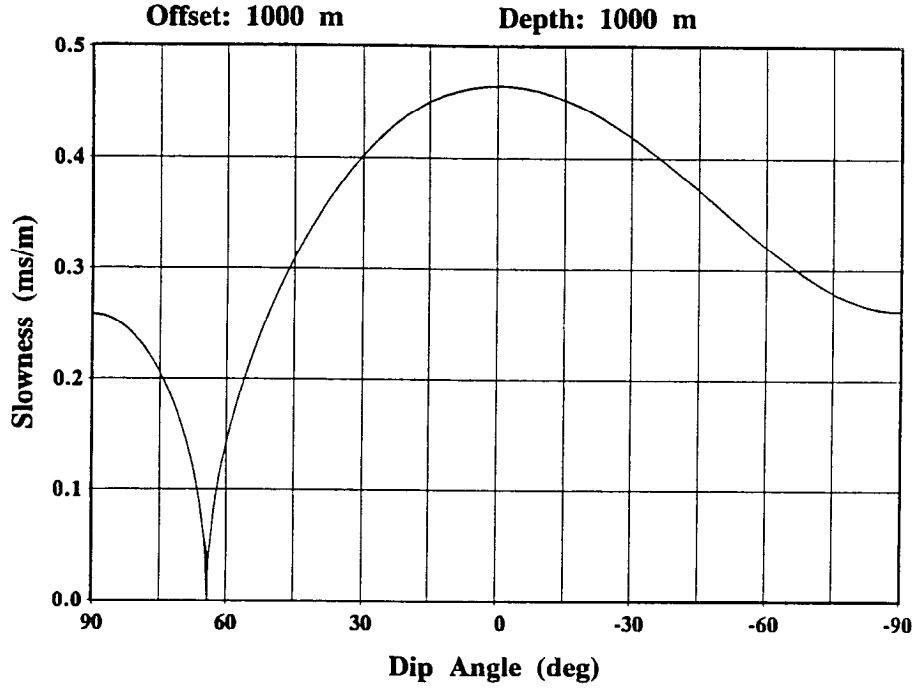


(b)

Fig. 3. Apparent P-SV slowness curves for a reflector depth of 1 km and source-to-receiver offsets of a) 0.5 km and b) 1.0 km.

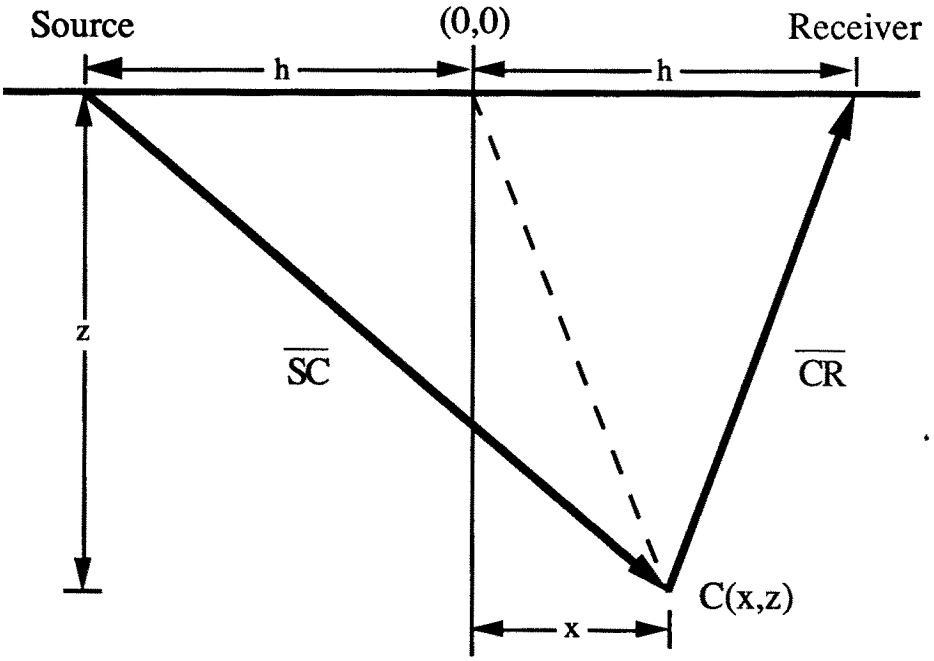


Fig. 4. Raypath geometry for computing the locus of points from which a datum sample could have originated.

## P-SV ZERO-OFFSET MAPPING

The first step in deriving the zero-offset mapping equation is to determine the locus of points from which any datum sample recorded at time **t** could have originated. Figure 4 shows the geometry now being considered, in which the origin of the coordinate system has been shifted to the midpoint location. The datum sample is assumed to have been converted at the point **C**, which is at depth **z** and horizontal distance **x** away from the midpoint. From the figure, it is seen that the total traveltime **t** must again be the sum of the traveltimes along the paths $\overline{SC}$ and $\overline{CR}$;

$$t = \frac{\overline{SC}}{\alpha} + \frac{\overline{CR}}{\beta} ,$$

or

$$t = \frac{\sqrt{(h+x)^2+z^2}}{\alpha} + \frac{\sqrt{(h-x)^2+z^2}}{\beta}$$

in the new coordinate system. Rationalization and simplification of this equation gives

$$\left(\frac{\alpha^2-\beta^2}{\alpha\beta}\right)^2\left(z^2+x^2+h^2\right)^2 - 2\left(\frac{\alpha^2+\beta^2}{\alpha\beta}\right)\left[\alpha\beta t^2+2h\left(\frac{\alpha^2-\beta^2}{\alpha\beta}\right)x\right]\left(z^2+x^2+h^2\right)$$

$$+\left[\alpha\beta t^2+2h\left(\frac{\alpha^2-\beta^2}{\alpha\beta}\right)x\right]^2 + 16x^2h^2 = 0 \quad . \qquad (11)$$

For the P-P case, where $\alpha = \beta = V$, it can easily be shown that equation 11 reduces to

$$\left(\frac{x}{a}\right)^2 + \left(\frac{z}{b}\right)^2 = 1$$

with

$$a = \frac{Vt}{2} \quad \text{and} \quad b = \frac{V\sqrt{t^2 - 4h^2/V^2}}{2} = \frac{Vt_0}{2},$$

showing the locus of possible origin to be an ellipse. Converting from depth **z** to two-way vertical traveltime gives the well-known migration ellipse for P-P data (e.g. Deregowski and Rocca, 1981). A plot of several of these ellipses for the P-P case, for a velocity of 3000 m/s and various two-way times, is shown in Figure 5.

For the P-SV case, equation 11 is of the form

$$A\xi^2 - 2B(x)\xi + C(x) = 0,$$

which is quadratic in the term

$$\xi = z^2 + x^2 + h^2.$$

The positive root of the equation gives unacceptable solutions for **z**, and is discarded. The remaining root simplifies to

$$z^2 + x^2 + h^2 =$$

$$(\alpha^2-\beta^2)^{-2}\left\{(\alpha^2+\beta^2)\left[\alpha^2\beta^2t^2+2h(\alpha^2-\beta^2)x\right] - 2\alpha^2\beta^2t\sqrt{\alpha^2\beta^2t^2+4h(\alpha^2-\beta^2)x}\right\} \qquad (12)$$

This equation generates the depth migration locus for a datum point recorded at time **t** and half-offset **h**, at a distance **x** away from the midpoint. Converting from vertical depth **z** to two-way vertical time $\tau$ where

$$\tau = \frac{z}{\alpha} + \frac{z}{\beta} = \left(\frac{\alpha+\beta}{\alpha\beta}\right)z,$$

equation 12 becomes

$$\tau^2 = (\alpha-\beta)^{-2}\left\{\left[\alpha^2\beta^2t^2+2h(\alpha^2-\beta^2)x\right]\left(\frac{\alpha^2+\beta^2}{\alpha^2\beta^2}\right) - 2t\sqrt{\alpha^2\beta^2t^2+4h(\alpha^2-\beta^2)x}\right\} - (x^2+h^2)\left(\frac{\alpha+\beta}{\alpha\beta}\right)^2$$

This result can be used to generate the raypath time migration curve for the single layer case, and could be used to implement a simple diffraction-summation-type prestack migration for P-SV data. A plot of several migration curves for $\alpha$=3000 m/s and $\beta$=1500 m/s and various values of **t** is shown in Figure 6. The location of the zero-dip conversion point as a function of two-way time (Tessmer and Behle, 1988) for the offset shown (1km) is overlaid on the figure, and is seen to correspond to the zero-dip maximum two-way time on each of the migration curves. The P-SV migration curves are asymmetric, with a shift in the direction of the receiver, whereas the P-P curves were seen to be ellipses, evenly centered on the source-to-receiver midpoint.

Next, it is necessary to construct the zero-offset response to the prestack migration curves given by equation 12. Zero-offset migration, when applied to this zero-offset response, should regenerate the original prestack migration curves. The operation that constructs this zero-offset response curve will be the DMO mapping function for P-SV data.

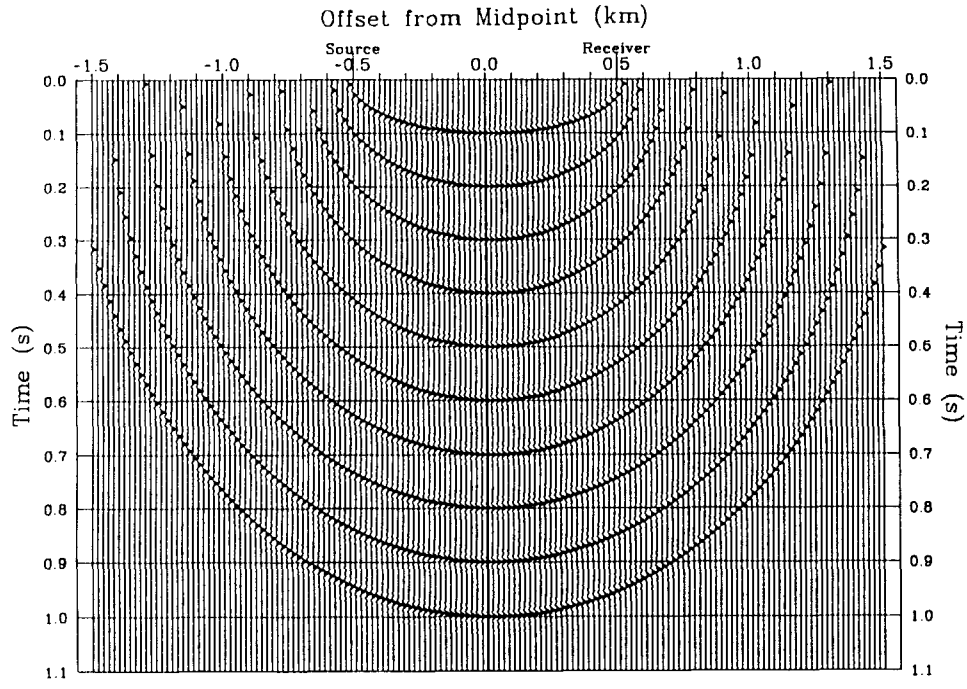


Fig. 5. P-P migration ellipses for a source-to-receiver offset of 1 km and various two-way times. The curves were generated by placing a spike of constant amplitude at the appropriate time-offset position, then filtering with a bandpass operator.

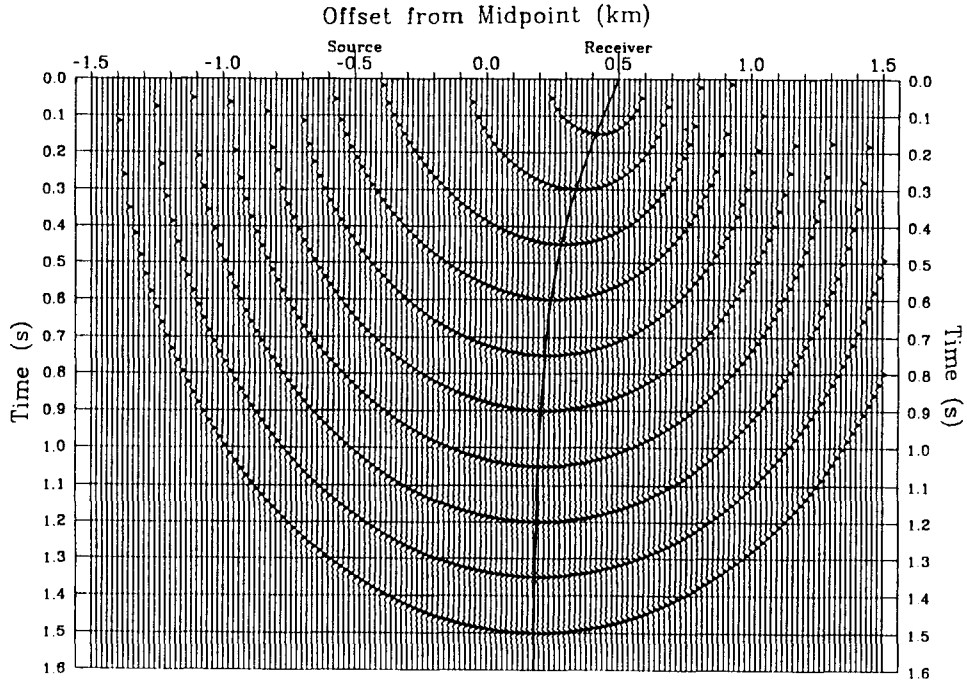


Fig. 6. P-SV migration curves for a source-to-receiver offset of 1 km and various two-way times. Curves were generated as in Figure 5.

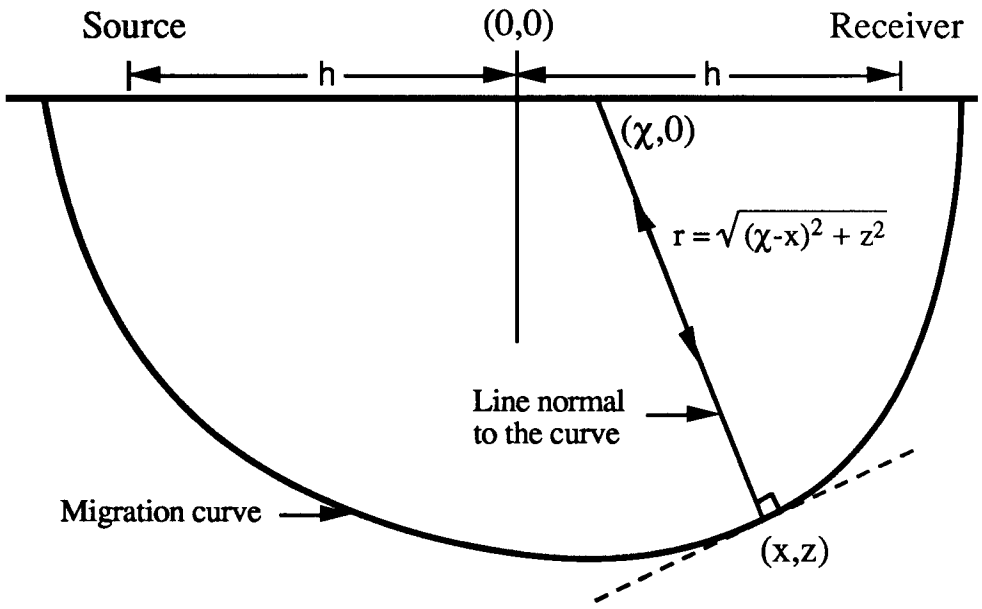


Fig. 7. Generation of the zero-offset response to a migration curve.

Figure 7 shows the geometry by which the zero-offset reflection response is generated. Normal-incidence reflection from any point (x,z) on the locus will be recorded at a point (χ,0) on the surface where the line normal to the locus at (x,z) emerges. The slope of the normal line is

$$s = -\frac{dx}{dz} = \frac{z}{x-\chi},$$

giving for $\chi(x)$

$$\chi(x) = x + z\frac{dz}{dx}. \tag{13}$$

Differentiating equation 12 w.r.t. x gives

$$z\frac{dz}{dx} = \frac{h}{(\alpha^2-\beta^2)}\left[(\alpha^2+\beta^2) - \frac{2\alpha^2\beta^2 t}{\sqrt{\alpha^2\beta^2t^2+4h(\alpha^2-\beta^2)x}}\right] - x.$$

Substitution of this result into equation 13 gives, after simplification,

$$\chi(x) = \frac{h}{(\alpha^2-\beta^2)}\left[(\alpha^2+\beta^2) - \frac{2\alpha^2\beta^2 t}{\sqrt{\alpha^2\beta^2t^2+4h(\alpha^2-\beta^2)x}}\right].$$

Rather than have $\chi$ as a function of x, the above equation can be inverted to give $x(\chi)$. This allows the computation of the x-distance away from the midpoint along the migration curve as a function of the offset from the midpoint along the DMO operator. The resulting equation is

$$x(\chi) = \frac{\alpha^2\beta^2t^2}{4h(\alpha^2-\beta^2)}\left[\frac{4\alpha^2\beta^2h^2}{[h(\alpha^2+\beta^2)-\chi(\alpha^2-\beta^2)]^2} - 1\right]. \qquad (14)$$

The distance **r** from the zero-offset conversion point (x,z) to the point ($\chi$,0) on the surface will be

$$r^2 = (\chi-x)^2 + z^2.$$

Substituting for **z** from equation 12 and **x** from equation 14, this reduces to

$$r^2 = (h^2-\chi^2)\left[\frac{\alpha^2\beta^2t^2}{2h[h(\alpha^2+\beta^2)-\chi(\alpha^2-\beta^2)]} - 1\right]. \qquad (15)$$

The zero-offset conversion time, $\tau_{p\text{-}sv}$, will be the time to travel from the surface to the conversion point at velocity $\alpha$, plus the time to travel back from the conversion point to the surface at velocity $\beta$, i.e.,

$$\tau_{p\text{-}sv} = \frac{r}{\alpha}+\frac{r}{\beta} = \left(\frac{\alpha+\beta}{\alpha\beta}\right)r. \qquad (16)$$

Substituting for **r** from equation 15, this becomes

$$\tau_{p\text{-}sv} = \left(\frac{\alpha+\beta}{\alpha\beta}\right)\sqrt{(h^2-\chi^2)\left[\frac{\alpha^2\beta^2t^2}{2h[h(\alpha^2+\beta^2)-\chi(\alpha^2-\beta^2)]} - 1\right]}. \qquad (17)$$

This equation gives the exact traveltime mapping function for the P-SV constant velocity DMO operator. For any offset $\chi$ away from the midpoint, it allows the computation of the time $\tau$ to which a point recorded at time **t** and half-offset **h** should be moved to apply the DMO correction, or to form the DMO operator. As with P-P DMO, the P-SV DMO curves are constrained to fall within a maximum distance of $\pm h$ away from the midpoint. For P-P reflection, with $\alpha = \beta = V$, equation 17 reduces to

$$\tau_{p\text{-}p} = \sqrt{t^2-\frac{4h^2}{V^2}}\sqrt{1-\frac{\chi^2}{h^2}} = t_0\sqrt{1-\frac{\chi^2}{h^2}}, \qquad (18)$$

where $t_0$ is the NMO-corrected time. This can be rearranged to give a second ellipse;

$$\left(\frac{\tau_{p\text{-}p}}{t_0}\right)^2+\left(\frac{\chi}{h}\right)^2 = 1.$$

This equation is the same expression for the P-P DMO operator given by Hale, 1988. Shown in Figure 8 are the DMO curves corresponding to the migration curves of Figures 5 and 6, computed using equations 17 and 18. The curves have all been truncated at the points corresponding to reflector dip of $\pm 90°$, as will be discussed next.

Equation 17 generates the shape of the DMO curve, but it is still necessary to determine the physical limits on $\tau_{p\text{-}sv}$. These limits will establish the minimum and maximum time values, corresponding to some maximum physical dip, that the DMO operator can take on at any offset $\chi$ away from the midpoint. This, in turn, will determine

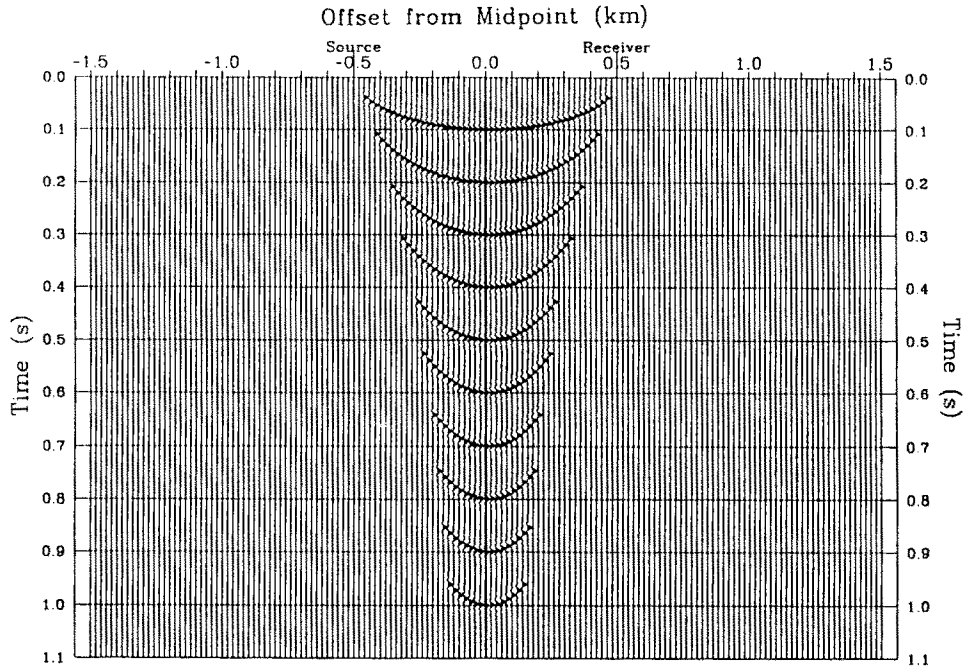


(a)

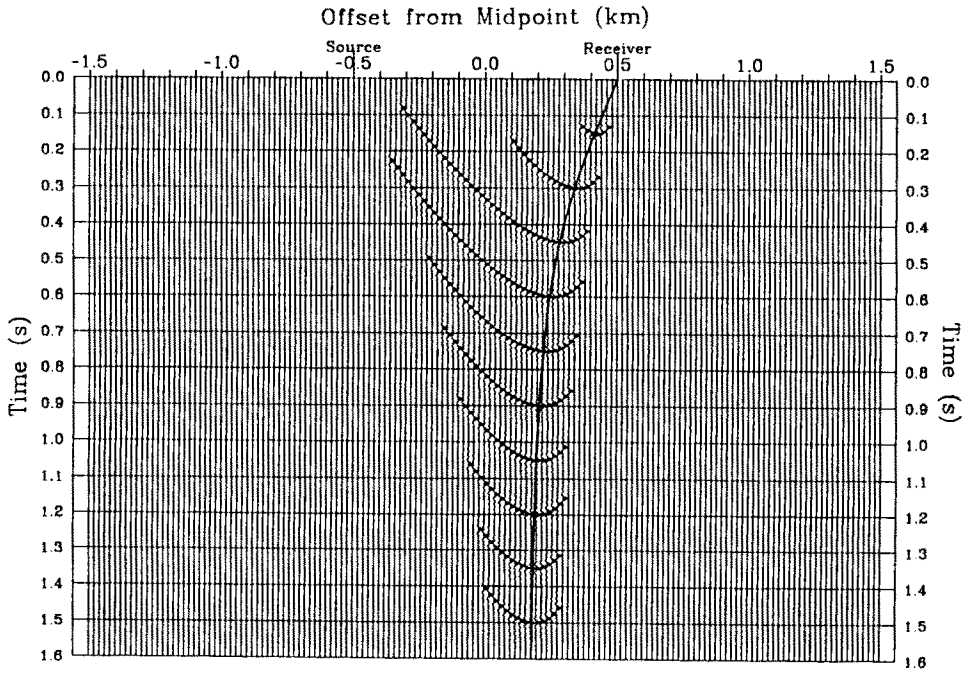


(b)

Fig. 8. DMO curves corresponding to the migration curves of a) Figure 5 (P-P) and b) Figure 6 (P-SV). Curves were generated as in Figure 5.

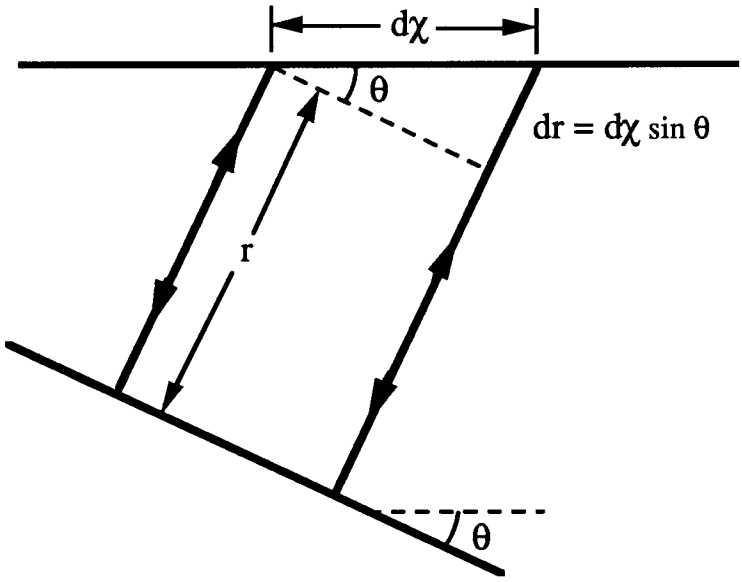


Fig. 9. Relationship between changes in zero-offset distance **r** and operator offset χ.

the envelope of the DMO operator. For fixed velocity, differentiation of equation 16 gives

$$d\tau = \left(\frac{\alpha+\beta}{\alpha\beta}\right) dr \quad . \tag{19}$$

From Figure 9, it is seen that

$$dr = d\chi \sin\theta \quad ,$$

which gives, from equation 19, that the slope **s** along the DMO curve is

$$s = \frac{d\tau}{d\chi} = \left(\frac{\alpha+\beta}{\alpha\beta}\right) \sin\theta \quad . \tag{20}$$

This result relates the dip angle at the point of conversion to the slope on the DMO operator. Equation 17 can be differentiated w.r.t. χ to give

$$s = \frac{1}{\tau}\left(\frac{\alpha+\beta}{\alpha\beta}\right)^2 \left\{ \chi + \frac{\alpha^2\beta^2 t^2}{4h} \frac{\alpha^2(h-\chi)^2 - \beta^2(h+\chi)^2}{\left[\alpha^2(h-\chi)+\beta^2(h+\chi)\right]^2} \right\} . \tag{21}$$

It is more convenient to have **s** defined in terms of τ, rather than **t** and τ. To do this, equation 17 can be inverted to give t(χ,τ);

$$t = \frac{1}{(\alpha+\beta)} \sqrt{\left[\tau_{p\text{-}sv}^2 + \left(\frac{\alpha+\beta}{\alpha\beta}\right)^2 (h^2-\chi^2)\right] \left\{ \frac{2h\left[h(\alpha^2+\beta^2) - \chi(\alpha^2-\beta^2)\right]}{h^2-\chi^2} \right\}} \quad . \tag{22}$$

This expression can be used to remove **t** from equation 21, with result

$$s = \frac{1}{2\tau}\left(\frac{\alpha+\beta}{\alpha\beta}\right)^2\left\{\frac{(\alpha^2-\beta^2)(h^2-\chi^2)^2 + \tau^2\left(\frac{\alpha\beta}{\alpha+\beta}\right)^2\left[\alpha^2(h-\chi)^2-\beta^2(h+\chi)^2\right]}{(h^2-\chi^2)\left[\alpha^2(h-\chi)+\beta^2(h+\chi)\right]}\right\}. \qquad (23)$$

This equation gives the slope s at any point $(\chi,\tau)$ on the DMO operator, which can, in turn, be used to compute the dip angle at that point using equation 21. Alternatively, if it is desired that only dip up to some maximum angle be passed by the operator, then the slope corresponding to that dip angle can be computed using equation 20. Equation 23 then gives a quadratic expression for $\tau$, with solution

$$\tau = (h^2-\chi^2)\left\{\frac{\left[\alpha^2(h-\chi)+\beta^2(h+\chi)\right]s \pm \sqrt{\left[\alpha^2(h-\chi)+\beta^2(h+\chi)\right]^2 s^2 - (\alpha^2-\beta^2)\left[\alpha^2(h-\chi)^2-\beta^2(h+\chi)^2\right]}}{\alpha^2(h-\chi)^2-\beta^2(h+\chi)^2}\right\}. \qquad (24)$$

The two values of $\tau$ give the minimum and maximum time that the operator can have at offset $\chi$ away from the midpoint. Ideally, the dip aperture of the DMO operator would be set to pass all possible dips (±90°). It is possible, however, that this will lead to spatial aliasing of the operator at large dip angles. When this occurs, the DMO dip aperture can be restricted to prevent aliasing (Beasley and Mobley, 1988) by using equation 24. As an example of this, Figure 10 shows two DMO operators that have been constrained to pass dips in the range of ±60° and ±30°. For the trace spacing and frequency content of the wavelet used in the figure, aliasing occurs for dips greater than 40°. This can be seen from the summed operator plot for the ±60° operator, in which the aliased dips produce visible artifacts. For very small dip apertures, the DMO operator collapses to just the trace itself, positioned along the conversion-point curve. P-SV DMO with a small dip aperture is therefore equivalent to performing a zero-dip conversion-point rebinning of the data.

At the location of the zero-dip conversion point, the slope s along the DMO curve is zero. At this point, $\chi$ is equal to the offset away from the midpoint of the zero-dip conversion point. Setting s to zero in equation 21 leads to the following cubic equation for $\chi$;

$$4h\left(\frac{\alpha^2-\beta^2}{\alpha\beta}\right)\chi^3 + \left(\frac{\alpha^2-\beta^2}{\alpha\beta}\right)\left[\alpha\beta t^2 - 8h^2\left(\frac{\alpha^2+\beta^2}{\alpha\beta}\right)\right]\chi^2$$

$$- 2h\left(\frac{\alpha^2+\beta^2}{\alpha\beta}\right)\left[\alpha\beta t^2 - 2h^2\left(\frac{\alpha^2+\beta^2}{\alpha\beta}\right)\right]\chi + \alpha\beta t^2 h^2\left(\frac{\alpha^2-\beta^2}{\alpha\beta}\right) = 0. \qquad (25)$$

It appears that all other equations for the conversion point location involve solving a quartic equation (e.g. Tessmer and Behle, 1988). The desired root to equation 25 can be found using standard methods. Defining

$$\eta = \frac{1}{6h}\left(\frac{\alpha\beta}{\alpha^2-\beta^2}\right)\left[\alpha\beta t^2 + 4h^2\left(\frac{\alpha^2+\beta^2}{\alpha\beta}\right)\right],$$

$$\rho = \frac{1}{2}\left[\eta - 2h\left(\frac{\alpha^2+\beta^2}{\alpha^2-\beta^2}\right)\right],$$

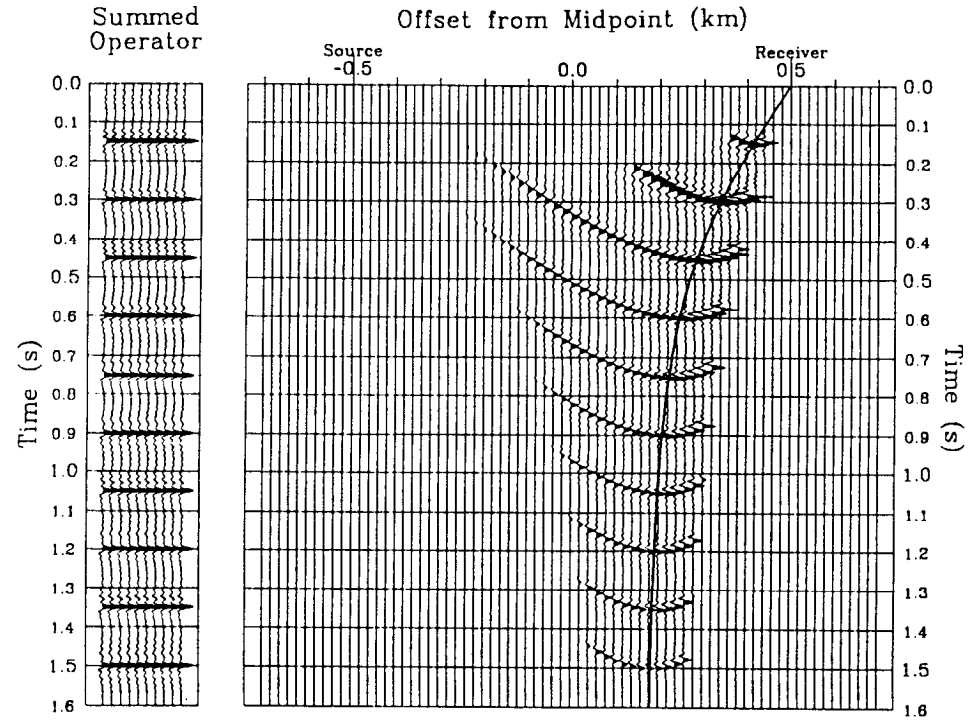


(a)

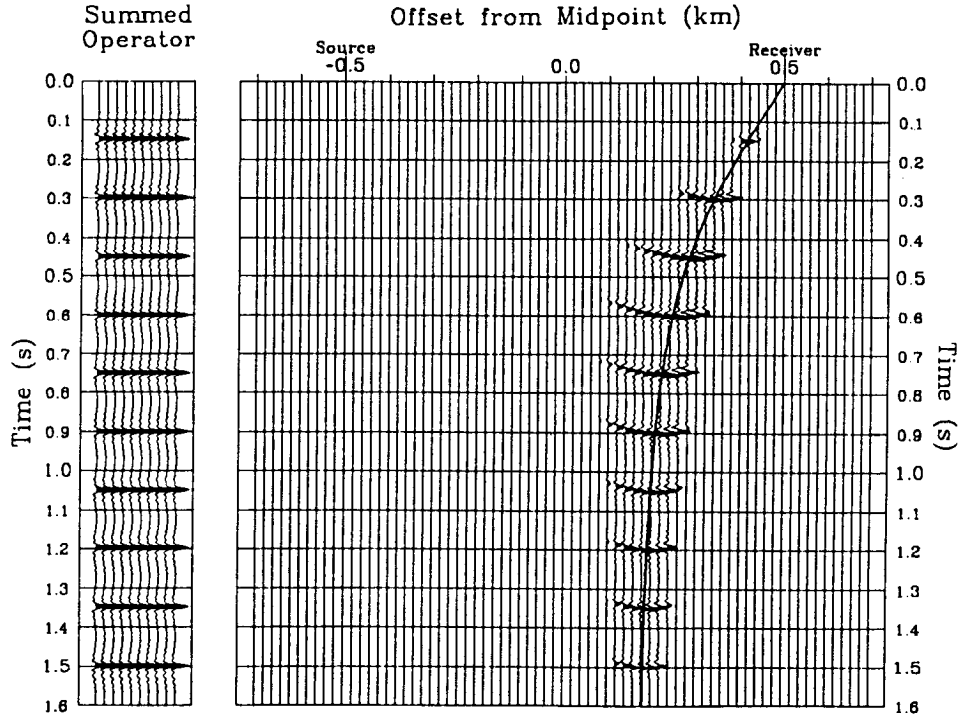


(b)

Fig. 10. DMO operators with dip apertures restricted to a) ±60° and b) ±30°.

$$b = h^2(\eta+\rho) + \rho\left(\frac{3\eta^2}{4} - \rho^2\right),$$

and

$$\Theta = \frac{1}{3}\left[\cos^{-1}\left(-\frac{4b}{\eta^3}\right) + 4\pi\right],$$

then the conversion point offset is given by

$$\chi = \eta \cos\Theta - \rho. \tag{26}$$

This result is found to give the same values for the conversion point location as are obtained using the equation given by Tessmer and Behle (1988).

## P-SV DMO APPLICATION

An integral-summation algorithm (Deregowski, 1985) was implemented to test the P-SV DMO equations on synthetic data. The algorithm consists of first constructing a time-domain DMO operator for each input trace, then summing the operators to get the final DMO result. The dip aperture was restricted to prevent operator aliasing at the maximum frequency of the input data. The operator amplitude weighting function used was based upon the approximate Fresnel width of the tangent to the DMO curve at every point, normalized to the width at zero dip. The operator phase correction was computed by numerically solving, for each time sample, a stationary-phase integral as a function of the operator width in wavelengths at that sample. To reduce computation time, only the phase correction for the dominant frequency of the data was estimated. This same phase correction was then applied to all frequencies of the data. The result of these amplitude and phase corrections can be seen in the operators shown in Figure 10. The NMO correction incorporated into equation 17 was removed from the DMO operator, allowing the application of DMO to data that has been previously NMO-corrected.

Table 1. Parameters used in generating the synthetic test data.

| | |
|---|---|
| Group interval | 25 meters |
| Source interval | 50 meters |
| Traces per record | 96 |
| Trace offsets | 25 m to 1200 m, 25 m increment split-spread records |
| Data bandwidth | 5-35 hz |
| P-wave velocity | 3000 m/s |
| S-wave velocity | 1500 m/s |

The synthetic data was constructed with the Uniseis modeling system, using the parameters given in Table 1. The model itself consists of two flat layers at depths of 1 and 2 km, as well as four dipping layers, having dips of 15, 30, 45, and 60 degrees. The total data volume was made up of 41 split-spread records of 96-trace data. In order to better assess the performance of the DMO operation, all AVO effects were initially removed from the data.

The result of stacking the data volume using the asymptotic approximation (Fromm, Krey, and Weist, 1985) is shown in Figure 11. From the figure, it is seen that the three most steeply-dipping reflectors have been attenuated, especially at shallow depth. Shown in Figure 12 is the result of stacking the data by true conversion point, accomplished by applying P-SV DMO with a very small dip aperture. It is seen that true CCP stacking gives greater attenuation of the dipping layers than does the asymptotic method. Figure 13 shows the result of applying P-SV DMO to the data using a dip aperture of 80°. Comparing this result to Figures 11 and 12, it is seen that there is less attenuation of the dipping reflectors. Figure 14 shows NMO-corrected gathers taken from the positions indicated at the top of Figures 11 and 13, first after asymptotic gathering, then after DMO has been applied in twelve common-offset planes. The dipping events on the asymptotic gathers are visibly overcorrected, whereas the events in the DMO gathers are nearly flat.

In reality, AVO affects are large in P-SV data. To evaluate the performance of P-SV DMO in a more realistic case, the model data was again processed with AVO effects left in. The result of stacking this second data set using the asymptotic binning method is shown in Figure 15, and the section obtained by applying P-SV DMO is shown in Figure 16. In this case, DMO is again seen to produce an improvement in the dipping events.

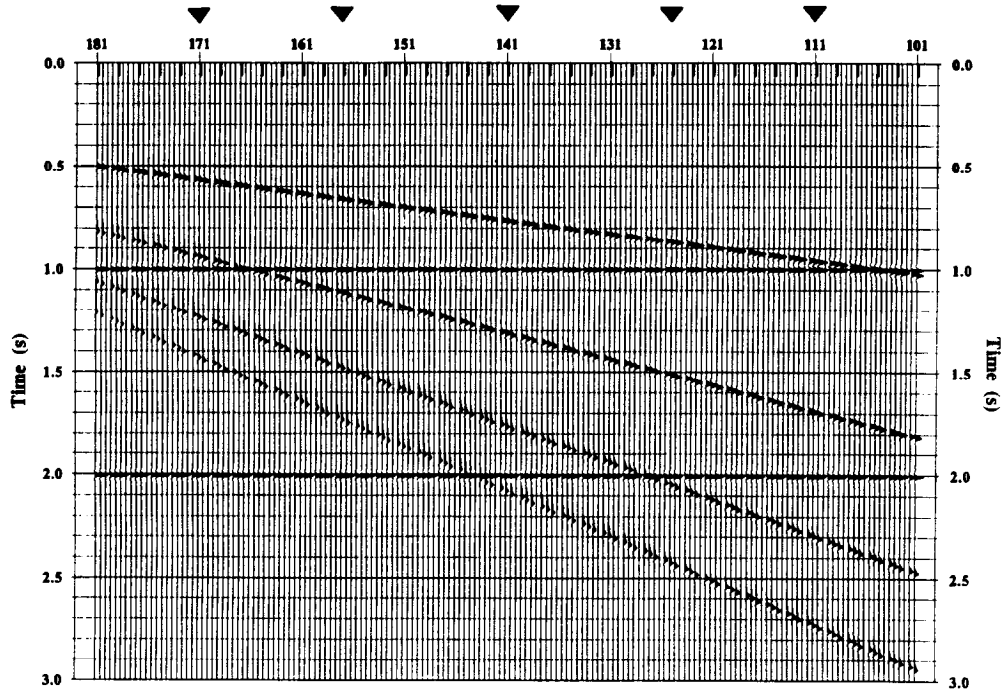


Fig. 11. Synthetic data stacked using the asymptotic gathering method.

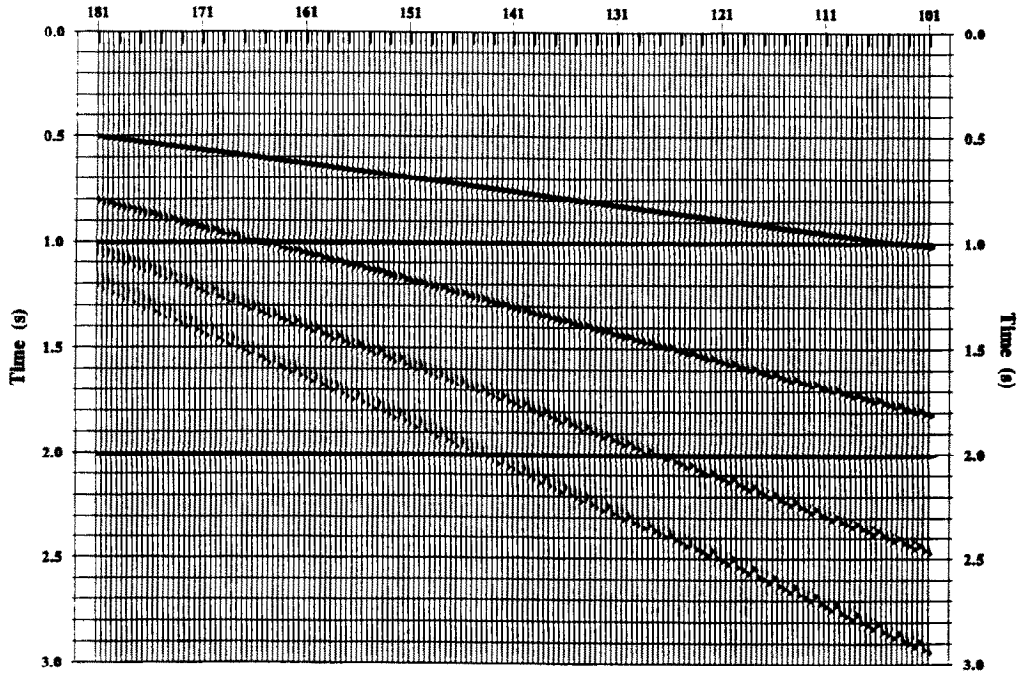


Fig. 12. Synthetic data stacked using true conversion-point gathering.

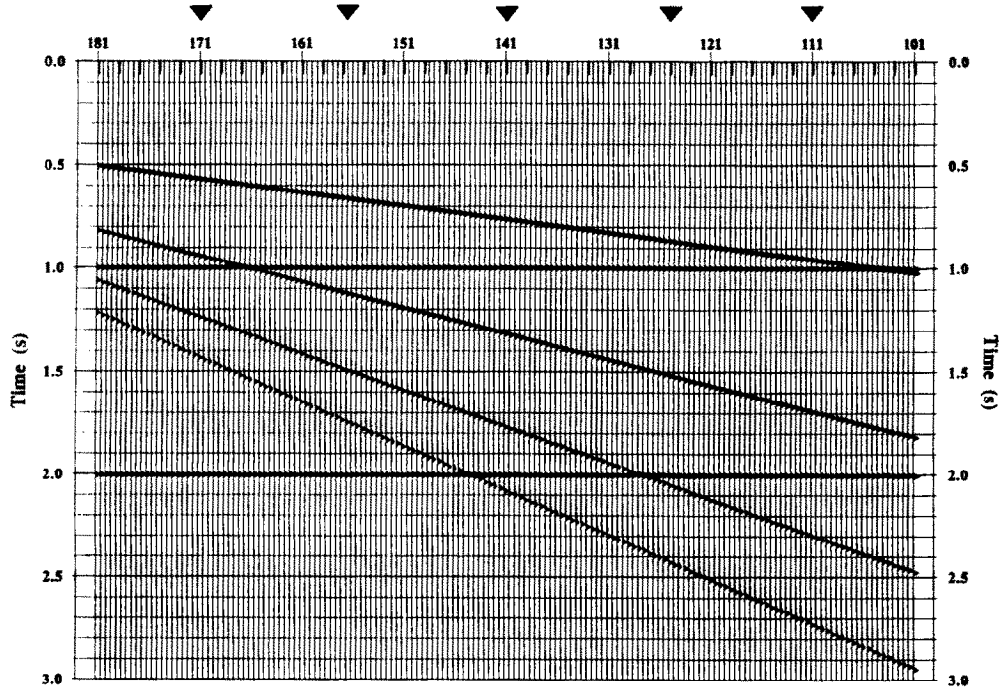


Fig. 13. Synthetic data stacked using P-SV dip moveout.

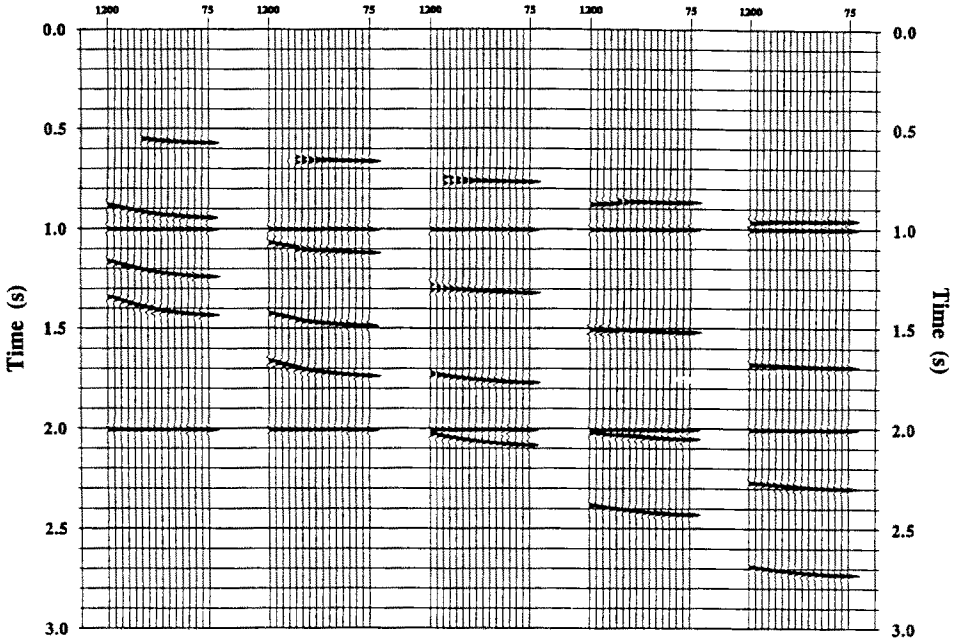


(a)

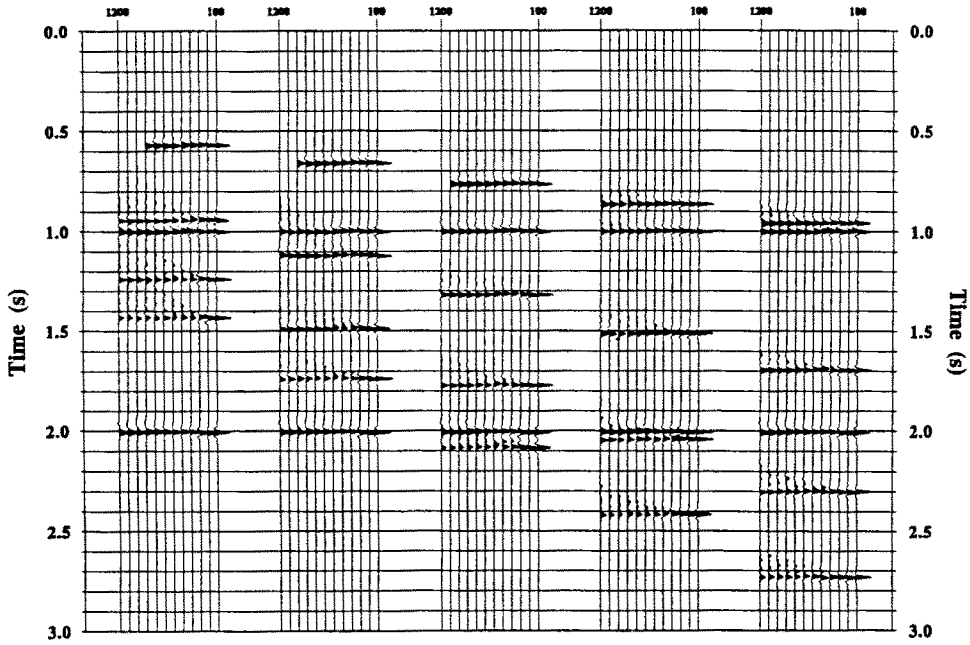


(b)

Fig. 14. NMO-corrected gathers after a) asymptotic gathering b) P-SV DMO.

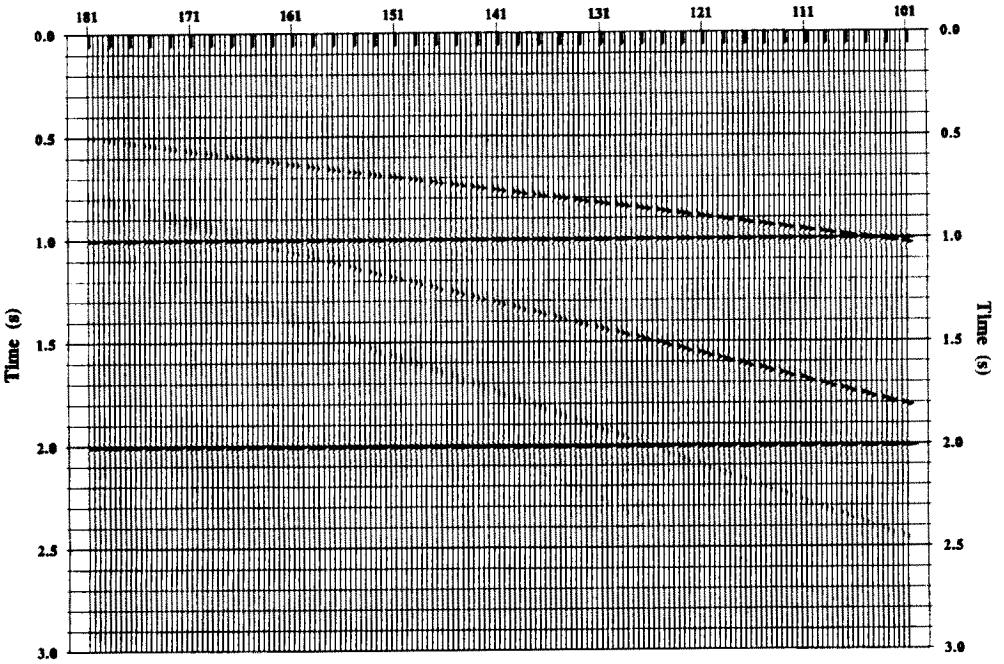


Fig. 15. AVO synthetic data stacked using the asymptotic gathering method.

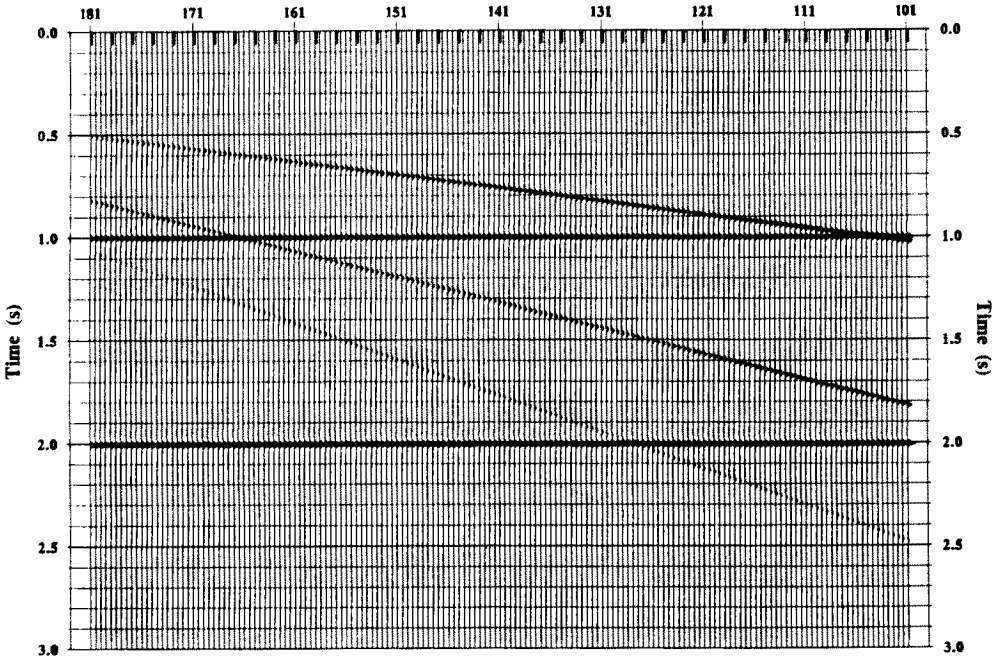


Fig. 16. AVO synthetic data stacked using P-SV dip moveout.

## DISCUSSION

From Figure 6, it can be seen that parts of the shallower migration curves actually correspond to conversion by transmission, rather than reflection. Because a seismic section is usually considered to be a reflection image, it may be desirable to suppress this part of the migration and DMO curves. In real data, however, the mute applied to elliminate early noise would also remove the data to which these curves would correspond, making suppression by other means unnecessary.

From equation 18, it is seen that P-P dip moveout factors into the product of a velocity-dependent term, $t_0$, and a velocity-independent term. This means that the application of DMO to NMO-corrected P-P data requires no velocity information, and is relatively insensitive to changes in velocity. It is not possible to factor equation 17 for P-SV DMO in a similar way. This means that P-SV DMO requires an estimate of both a compressional and a shear velocity, making it more sensitive to velocity errors than is P-P DMO.

The velocity dependance of equation 17 can be broken down into two main parts; NMO and conversion-point binning. First, the DMO equation is applying a single-layer NMO correction to the input data. At the location of the zero-dip conversion point, equation 17 reduces to an exact NMO equation for the single-layer P-SV case. By using equation 26 to first compute the conversion-point location, the NMO correction that is being applied to the data can be calculated. This correction can then be removed from the DMO operation, so that P-SV DMO is actually applied to NMO-corrected gathers, as in the P-P case. This removes some of the problems involved in applying single-layer DMO to multi-layer data, and makes the DMO operation less sensitive to velocity estimation.

The second place where velocity dependence occurs is in the movement of datum samples by DMO about the zero-dip conversion point, rather than the midpoint. Because the location of the conversion point is velocity dependant, errors in velocity estimation will affect the horizontal positioning of the DMO'd data. To reduce the problem, as well as allow for a more appropriate conversion-point binning of the data, it is possible to pre-bin the input data using a more exact method into a series of common-offset planes. Then, just as the NMO is removed from the DMO process, the conversion-point rebinning that is carried out by the operator could be computed and removed. DMO would then be applied to gathers that have been both NMO-corrected and CCP binned, and would form the DMO curves around the current time and horizontal position of the datum samples. This should further reduce the velocity dependence of P-SV DMO, and improve its applicability to multi-layer data.

It is interesting to note that asymptotic binning appears to better preserve dipping data than does true CCP stacking, as can be seen from Figures 11 and 12. This appears to be due to the decrease in CCP dispersal produced by the asymptotic approximation for data converted from positive-dip interfaces. Although there is a corresponding increase in the dispersal for negative-dip data, the dispersal for positive dips is significantly greater than for negative dips, as can be seen from Figure 2. The overall result appears to be a net decrease in the attenuation of dipping layers that have been gathered and stacked using the asymptotic method.

## CONCLUSIONS

Expressions for P-SV dispersal and apparent stacking slowness within a CCP gather were derived. It was found that both the dispersal and apparent velocity are asymmetric about zero-dip, indicating that P-P dip moveout is not appropriate for P-SV data. A formulation of the traveltime mapping equation for the P-SV DMO impulse response for a single-layer case was derived by using geometrical optics. It was shown that, as in the P-P case, an exact solution to the time response curves for a P-SV DMO operator can be obtained. This solution contains within it the P-P DMO traveltime equation as a special case. Time-response curves for a P-SV DMO operator were generated using this equation, and showed the DMO curves to be asymmetric, with the location of maximum time corresponding to the position of the conversion point. Application of P-SV DMO moves the data to the horizontal conversion point, performing conversion-point rebinning. A new method for computing the location of the zero-dip conversion point was presented. An integral-summation algorithm for P-SV DMO was implemented, and was found to give a visible improvement in the amplitude and continuity of dipping events.

## ACKNOWLEDGEMENTS

I would like to thank Rob Stewart for suggesting this research topic, and for his continued interest in this work. Also, the support of the sponsors of the CREWES project is very much appreciated.

## REFERENCES

Beasley, C., and Mobley, E., 1988, Amplitude and anti-aliasing treatment in (x,t) domain DMO: presented at the 58th Ann. Internat. Mtg., Soc. Explor. Geophys.

Deregowski, S.M., and Rocca, F., 1981, Geometrical optics and wave theory of constant offset sections in layered media: Geophys. Prosp., v. 29, 384-406.

Deregowski, S.M., 1982, Dip-moveout and reflector point dispersal: Geophys. Prosp., v.30, 318-322.

Deregowski, S.M., 1985, An integral implementation of dip moveout: Presented at the 47th Ann. Mtg., EAEG.

Hale, D., 1984, Dip moveout by Fourier transform: Geophysics, v. 49, 741-757.

Hale, D., 1988, Dip moveout processing: Soc. Explor. Geophys. course notes.

Fromm, G., Krey, Th., and Wiest, B., 1985, Static and dynamic corrections, in Dohr, G. Ed., Seismic Shear Waves: Handbook of Geophysical Exploration, v. 15a, 191-225.

Judson, D.R., Schultz, P.S., and Sherwood, J.W.C., 1978, Equalizing the stacking velocities of dipping events via DEVELISH: presented at the 48th Ann. Internat. Mtg., Soc. Explor. Geophys.

Levin, F.K., 1971, Apparent velocity from dipping interface reflections: Geophysics, v. 36, 510-516.

Notfors, C.D., and Godfrey, R.J., 1987, Dip moveout in the frequency-wavenumber domain: Geophysics, v. 52, 1718-1721.

Tessmer, G., and Behle, A., 1988, Common reflection point data-stacking technique for converted waves: Geophysical Prospecting, v. 36, 661-688.

Yilmaz, O., and Claerbout, J.F., 1980, Prestack partial migration: Geophysics, v. 45, 1753-1779.